Carbon Nanotube Strain Sensor Based Hemoretractometer for Blood Coagulation Testing

Zida Li,[†] Yize Wang,[†] Xufeng Xue,[†] Brendan McCracken,[‡,§] Kevin Ward,[‡,§] and Jianping Fu*[,†,§,∥,⊥]

[†]Department of Mechanical Engineering, [§]Michigan Center for Integrative Research in Critical Care, and [∥]Department of Biomedical Engineering, University of Michigan, Ann Arbor, Michigan 48109, United States

[‡]Department of Emergency Medicine and [⊥]Department of Cell and Developmental Biology, University of Michigan Medical School, Ann Arbor, Michigan 48109, United States

Ⓢ Supporting Information

ABSTRACT: Coagulation monitoring is essential for perioperative care and thrombosis treatment. However, existing assays for coagulation monitoring have limitations such as a large footprint and complex setup. In this work, we developed a miniaturized device for point-of-care blood coagulation testing by measuring dynamic clot retraction force development during blood clotting. In this device, a blood drop was localized between a protrusion and a flexible force-sensing beam to measure clot retraction force. The beam was featured with micropillar arrays to assist the deposition of carbon nanotube films, which served as a strain sensor to achieve label-free electrical readout of clot retraction force in real time. We characterized mechanical and electrical properties of the force-sensing beam and optimized its design. We further demonstrated that this blood coagulation monitoring device could obtain results that were consistent with those using an imaging method and that the device was capable of differentiating blood samples with different coagulation profiles. Owing to its low fabrication cost, small size, and low consumption of blood samples, the blood coagulation testing device using carbon nanotube strain sensors holds great potential as a point-of-care tool for future coagulation monitoring.

KEYWORDS: blood coagulation, carbon nanotube, strain sensor, clot retraction force, point-of-care diagnostics
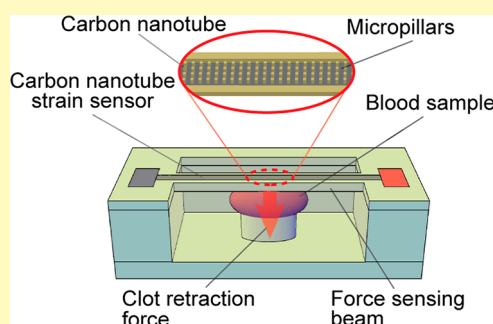
R obust, rapid, and timely monitoring of coagulation is of critical value in perioperative care and thrombosis treatment.[1] For example, in surgeries such as cardiopulmonary bypass, coagulation monitoring provides important information that can guide hemostatic therapy and minimize the need for blood transfusion.[2] Conventional coagulation tests, such as prothrombin time (PT) and activated partial thromboplastin time (aPTT), generally use plasma and thus do not provide information on the function of cellular components of the blood. The overall stability of a formed thrombus also cannot be assessed, since assays are terminated before fibrin is polymerized by Factor XIIIa.[1]

Commercially available devices of whole blood coagulation tests based on viscoelasticity alteration during clotting, such as thromboelastography (TEG), rotational thromboelastometry (ROTEM), and Sonoclot, are capable of assessing the function of both cellular and plasmatic components in both clotting and fibrinolysis. Indeed, these tests have been gaining acceptance in various clinical settings.[3] Nonetheless, these tests have limitations such as a large instrument size and high requirement for maintenance and personnel training.[3] The large blood volume consumption for TEG and ROTEM (∼340 µL) is also problematic for repetitive tests on pediatric patients.

Microtechnology holds the promise of developing mini-aturized assays with the merits of minimal blood consumption and high-assay throughput. Based on the same measurement principles as TEG, ROTEM, and Sonoclot, microengineered devices assessing viscoelasticity alteration during blood clotting using a magnatoelastic transducer,[4] quartz crystal micro-balance,[5] acoustic resonator,[6] ultrasound radiation,[7] laser speckle rheology,[8] cantilever beam oscillation,[9] dielectric sensor,[10] etc. have been reported. With the use of micro-technology, a few microscale devices have been specifically developed for platelet contractile force measurements down to the single cell level based on micropost array,[11] atomic force microscopy,[12] micropatterned fibrinogen array,[13] traction force microscopy,[14] etc. These devices are believed to be capable of monitoring the contractile function of platelets and thus identifying the cause of bleeding and guiding pro and anticoagulant therapies.[3] However, all these existing microscale devices were designed primarily for mechanistic study and showed limited potential for clinical applications.[15]

Herein we aimed to develop a miniaturized device for a point-of-care coagulation assay that accounts for both the mechanical rigidity of a fibrin network and platelet contraction. In our previous work, we developed a device, named
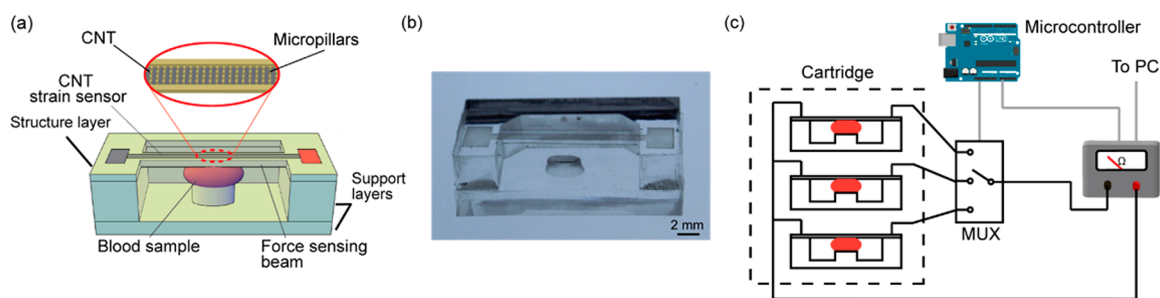
Figure 1. (a) Schematic of the CNT−mHRM device. The device was assembled from three parts, with the CNT strain sensor residing on the top PDMS thin beam. The bottom support layer contained a protrusion that held the blood sample along with the PDMS beam. The clot retraction force deformed the PDMS beam, leading to a change in the resistance of the CNT strain sensor. (b) Photograph of the CNT−mHRM device. (c) Schematic of the data acquisition setup. The cartridge housed multiple devices, and the multiplexer (MUX) routed the ohmmeters to the measured device. The microcontroller synchronized the MUX switching and ohmmeter data acquiring.
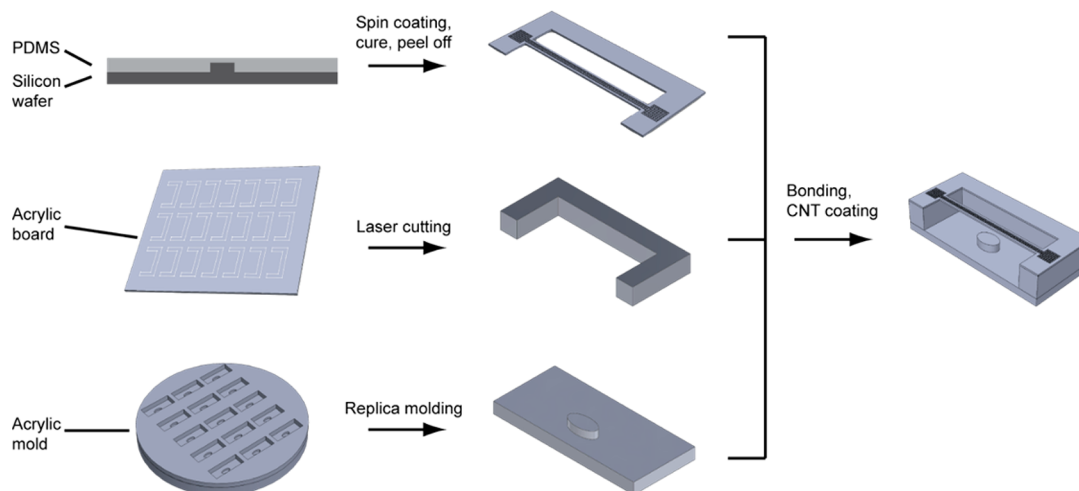

Figure 2. Fabrication process of CNT−mHRM devices. The top layer was fabricated by photolithography and soft lithography. The resultant PDMS beam had micropillar arrays to assist with CNT deposition. The middle layer was made of acrylic through layer cutting. The bottom layer was fabricated by PDMS replica molding. The devices were assembled through plasma bonding.

miniaturized HemoRetractoMeter (mHRM), based on image acquisition and analysis to measure the clot retraction force (CRF) generated during blood clotting and validated its performance for blood coagulation diagnosis.[16] To equip mHRM with electrical readout and miniaturize necessary data acquisition setup, in this work we integrated a carbon nanotube (CNT) strain sensor onto the force-sensing beam of the mHRM to achieve label-free, real-time CRF measurements (CNT−mHRM). In particular, we adopted a fixed protrusion and a membrane-like PDMS force-sensing beam to localize blood samples. CNT strain-sensing films were deposited onto the PDMS beam featured with micropillar arrays, which assisted uniform CNT coating.[17] We characterized electromechanical properties of the force-sensing beam and optimized its design, including the CNT solution concentration and geometries of the force-sensing beam. When tested with whole blood samples, the CNT−mHRM device generated results that were consistent with the imaging method and successfully captured different coagulation profiles of blood samples treated with either pro or anticoagulants. Together, the CNT−mHRM device holds great potential for point-of-care blood coagulation testing as an in vitro diagnostic tool.

■ EXPERIMENTAL SECTION

Preparation of CNT Solution. CNT solution was prepared as previously described.[17] Briefly, carboxyl-functionalized multiwalled carbon nanotubes (length: 1 μm, inner diameter: 7.5 nm, outer diameter: 10 nm; Cheap Tubes Inc.) were dispersed in deionized water at a concentration of 5 mg/mL using a probe sonicator (Model VCX130, Sonics & Materials Inc.). Solutions containing dispersed CNT were then centrifuged at 1000g for 10 min with resultant supernatant extracted as stock CNT solution for later use (Figure S1).[18] The final CNT concentration in stock CNT solution was 1.616 ± 0.083 mg/mL, as measured by weighing the precipitated CNT after complete water evaporation.

Device Design and Fabrication. The CNT−mHRM device was composed of three layers. The CNT strain sensor resided in the membrane-like, PDMS-made top layer, which was affixed to a rigid, acrylic-made middle layer (Figure 1a,b). The bottom layer was designed with a protrusion at its center, providing a locus to hold blood samples to be assayed.

Fabrication of the mHRM device involved laser cutting of an acrylic sheet and replica molding of PDMS. Laser cutting was conducted with a laser cutter system (VLS6.60, Universal Laser Systems). Cutting patterns were designed in AutoCAD (Autodesk, Inc.); laser power and cutting speed were determined from the user manual based on the thickness of acrylic sheet. Replica molding of PDMS started with mixing the PDMS base with the curing agent at certain ratios. The mixture was then degassed for 30 min to remove air bubbles before being poured on the molds. The molds with PDMS were then degassed again before being baked at 60 °C overnight. Cured PDMS

was then peeled off from the molds. Base-to-curing agent ratios of 10:1, 15:1, and 20:1 generated PDMS blocks with Young's moduli of 1.717 ± 0.034, 0.615 ± 0.009, and 0.301 ± 0.009 MPa, respectively, as measured by an Instron tensile testing machine (Illinois Tool Works Inc.).

The middle layer was acrylic shaped by laser cutting. The bottom layer was made of PDMS (10:1 base-to-curing-agent ratio) by replica molding, while the mold was acrylic that was also shaped by laser cutting (Figure 2).

The top layer was featured with micropillar arrays to facilitate CNT coating in the following steps. The micropillars were of square shape with 100 μm sides, and the gap size between adjacent pillars was also 100 μm. The top layer was fabricated by soft lithography of PDMS using silicon masters. Briefly, a silicon wafer was patterned through photolithography and deep reactive ion etching before it was silanized and spin-coated with PDMS base and a curing agent mixture. Spin coating was conducted at either 400 or 600 rpm for 1 min, resulting in PDMS membranes with thicknesses of 174.3 ± 4.37 or 105.0 ± 1.0 μm, respectively, as measured with a stylus profilometer (Dektak XT, Bruker Corporation). The spin-coated PDMS was then baked and peeled off as aforementioned. Ridges were designed along the beam outline, and a scalpel was used to cut out PDMS beams along the ridges. The length and width of the beams were 15 and 2.6 mm, respectively.

The three layers were assembled by chemically bonding acrylic and PDMS layers. Briefly, acrylic surfaces were treated with oxygen plasma (Model PDC-001, Harrick Plasma) for 1 min before being immersed in 1% (3-aminopropyl)triethoxysilane (APTES) for 1 h and air-dried. The PDMS surface was treated with oxygen plasma for 1 min before being put in contact with APTES-functionalized acrylic. The assembly was then baked at 60 °C for 1 h to assist chemical bonding.[19] The micropillar arrays were then treated with oxygen plasma for 3 min to make the PDMS surface hydrophilic before 1.5 μL of CNT solution, with a concentration of either 1.62, 1.21, or 0.81 mg/mL, was dispensed at a corner of the micropillar array and spread over the micropillar array evenly. The device was then placed in a vacuum chamber to accelerate water evaporation and minimize CNT aggregation (Figure S1).[20] The resultant carbon nanotube film displayed good uniformity, with individual fibers in contact with neighboring fibers without forming large bundles.[17]

Device Characterization. Devices were characterized to obtain the spring constant and gauge constant of the force-sensing beam. As shown in Figure S2, a probe force transducer (Model 400A, Aurora Scientific Inc.), which was mounted on a translation stage, was used to measure applied force. While the probe was approaching and deforming the beam at its center, the applied force was recorded from the force transducer while the beam displacement was recorded using the translation stage. A digital multimeter (Model 34401A, Agilent Technologies) was used simultaneously to measure the resistance of the CNT resistor. Conductive grease (Model 846, MG Chemicals) was applied on both ends of the CNT resistor to minimize contact resistance.

Data Acquisition. Multiplex data acquisition during blood coagulation testing was achieved by using an analog switch connected to the digital multimeter (Figure 1c). The digital multimeter was then connected to a computer via a GPIB Instrument Control Device (Model GPIB-USB-HS, National Instruments) and controlled by a LabVIEW program. A multiplexer (CD4051BE, Texas Instruments), controlled by a microcontroller (Arduino Uno, Arduino Company), was used to implement the analog switch circuit. Switch shifting led to transient connection of different devices to the multimeter for resistance measurements. Triggering signals were also sent by the microcontroller to the digital multimeter to synchronize resistance acquistion and switch shifting. The duration of a switch cycle was typically a few seconds depending on the number of devices being tested.

A cartridge was designed to house multiple mHRM devices for multiplex testing. Lead wires were embedded in the cartridge and projected into loading spots for quick device connection. Images were

acquired using a digital microscope (Dino-Lite Hand-held Digital Microscope, AnMo Electronics Co.).

Blood Specimen and Coagulation Assays. Whole blood was collected from human volunteers into a vacutainer (BD Vacutainer, BD Company) containing 3.2% sodium citrate under an IRB protocol approved by the University of Michigan (HUM00067675: Non-invasive Monitoring of the Critically Ill and Injured Patient). All blood samples were tested within 4 h after blood collection. For blood samples treated with pro or anticoagulants, aprotinin (80 μg/mL; Sigma-Aldrich Co.) or heparin (8 U/mL; Sigma-Aldrich Co.) were added into the blood and incubated in room temperature for 1 h before being assayed with CNT−mHRM devices.

At the beginning of blood coagulation tests, 20 μL of blood sample was suspended between the protrusion and the PDMS beam using a micropipette. A volume of 1.2 μL of CaCl$_2$ (0.2 M, Fisher Scientific) was then added into the blood droplet with gentle mixing. A Petri dish was used to cover the cartridge to alleviate evaporation before resistance acquisition was started. Image acquisition was also started when applicable. All assays were performed at room temperature (23 °C), and each device was used only once.

Data Analysis. The original data, which was a time series of electrical resistance, was smoothed with an FFT filter in Origin (OriginLab Corp.). Smoothed resistance data was then converted to CRF. To obtain key coagulation parameters, including reaction time T_r and CRF growth rate G_{CRF}, CRF data in the contraction development phase was fitted to a quadratic function. Specifically, T_r was defined as the time when CRF started to increase from a baseline level (CRF = 0), and CRF growth rate G_{CRF} was defined as the CRF growth rate at T_r. A two-sample unpaired Student's t test was performed in Origin for statistical analysis.

An image-processing program was designed and implemented in Python to analyze beam displacements in captured videos. Briefly, regions of beam centers were selected, and their outlines were analyzed by edge detection to obtain displacements of beam centers relative to their original locations. Beam displacements were then converted to CRF by multiplying beam displacements with its spring constant.

■ RESULTS

CNT−mHRM Device Design and Data Acquisition. The CNT−mHRM consisted of three parts: a structure layer and two support layers (Figure 1a,b). The structure layer mainly consisted of a thin PDMS beam featured with micropillar arrays, made from soft lithography (see Experimental Section). The PDMS beam was plasma-treated to render it hydrophilic before CNT solution was dispensed onto it and spread over the surface evenly. Owing to capillary force induced by the micropillars, CNT was uniformly deposited on the PDMS beam.[17] The deposited CNT film possessed good piezo-resistivity, making it suitable to serve as a strain sensor. In contact with the PDMS beam layer was an acrylic block, whose Young's modulus was about 2 GPa,[21] more than 1000 times higher than PDMS. Such high stiffness of the acrylic layer minimized PDMS beam deformation induced by factors other than CRF. The bottom support layer was designed with an elliptic cylinder protrusion aligned with the center of the PDMS force-sensing beam to localize blood samples to be assayed. The three parts were assembled through plasma bonding (Figure 2).

During blood coagulation testing, a drop of citrated blood, typically with a volume of 20 μL, was suspended between the PDMS force-sensing beam and the elliptical cylinder protrusion by pipetting before CaCl$_2$ solution was added to the suspended blood drop with gentle mixing. Recalcification of blood sample triggered blood coagulation, which induced clot retraction that pulled the PDMS force-sensing beam toward the elliptic
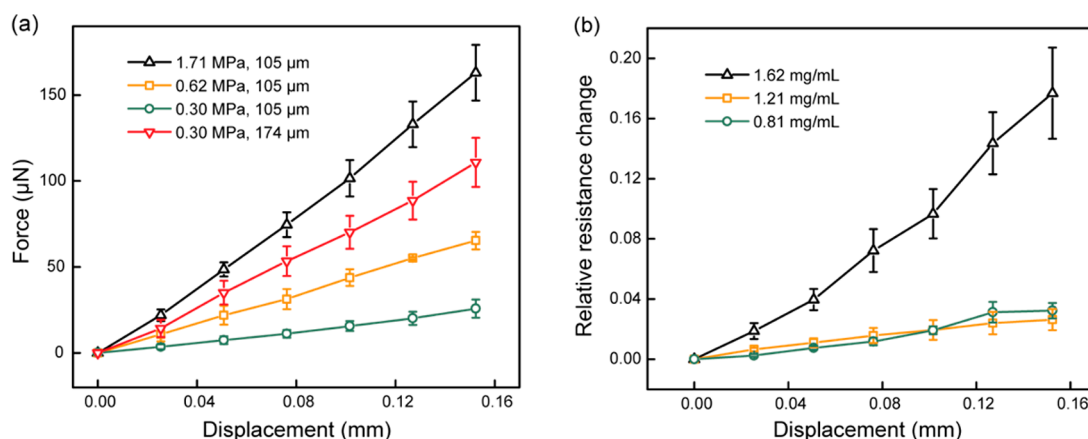
Figure 3. Characterization of CNT−mHRM devices. (a) The applied force plotted as a function of displacement of the center of the beams, with beams fabricated using PDMS with different Young's moduli (MPa) and different thicknesses (μm) as indicated. (b) Relative resistance change plotted as a function of displacement of the center of the beams, with the CNT strain sensor fabricated using CNT solutions of different concentrations as indicated.

cylinder protrusion and thus deformed the CNT strain sensor film. This deformation induced change in the electrical resistance of the CNT strain sensor. By monitoring the resistance change of the CNT strain sensor, CRF exerted on the PDMS membrane due to blood clotting could be monitored. To achieve multiplex testing, we designed a cartridge to house up to 10 CNT−mHRM devices, along with a circuit with an analog switch controlled by a microcontroller (Figure 1c). The analog switch routed the multimeter to collect resistance data from each CNT−mHRM device at different time points. Thus, multiplexed blood coagulation testing could be achieved, which greatly improved assay throughput.

Device Characterization. We designed experiments to characterize the relationship between the resistance change of the CNT strain sensor and CRF exerted on the PDMS force-sensing beam (Figure S2). Here, CNT−mHRM devices were first affixed on an optical table, and a probe force transducer, which was mounted on a linear translation stage, approached the center of the PDMS beam and displaced it. The amount of applied force, beam displacement, and resistance change of the CNT strain sensor were recorded from the force transducer, translation stage, and multimeter, respectively.

The relationship between applied force and beam displacement can be described by the beam spring constant as $K = F/\Delta x$, where K is the spring constant, F is applied force, and Δx is beam displacement. At a given force, smaller spring constant leads to greater beam displacements and thus a higher measurement sensitivity. From the classical beam theory,[16] the beam spring constant K is calculated as $K = 16E\delta^3 W/L^3$, where E is the Young's modulus of PDMS, and δ, W, and L are the beam thickness, width, and length, respectively. Given their small geometries, micropillars on the PDMS force-sensing beam had negligible impact on the beam spring constant K. Also, it is evident that the beam spring constant K can be conveniently adjusted by modulating the ratio of the PDMS base-to-curing agent (which results in PDMS layers with different Young's moduli) and spinning speed during spin coating of PDMS (which results in PDMS layers with varied thicknesses; see Experimental Section).

We first examined the effect of the Young's modulus of PDMS on the beam spring constant while maintaining its thickness at 105 μm. As expected, force exerted by the force

transducer exhibited a clear linear dependence on beam displacement (Figure 3). Force-sensing beams fabricated using softer PDMS had lower spring constants. Specifically, PDMS with Young's moduli of 1.71, 0.62, and 0.3 MPa resulted in force-sensing beams with spring constants K of 1.16 ± 0.37, 0.343 ± 0.034, and 0.158 ± 0.012 μN/μm, respectively. Thus, the Young's modulus of PDMS and the beam spring constant K showed a strong linear correlation (Figure S3a), consistent with the classical beam theory.

We further examined the effect of beam thickness on the beam spring constant. The spring constant K of PDMS beams with a thickness of 174 μm was 0.732 ± 0.117 μN/μm, four times greater than that of beams with a thickness of 105 μm (0.158 ± 0.012 μN/μm; Figure S3b). The smallest PDMS beam thickness was limited by our fabrication process. When the PDMS beam thickness was lower than 105 μm, the beam became fragile and difficult to manipulate.

Our data further showed that the relative resistance change of the PDMS force-sensing beam increased with its displacement in a linear manner.[17] To characterize the electromechanical properties of the PDMS force-sensing beam, a gauge constant (GC) was defined as the ratio of relative resistance change to beam displacement as $GC = (\Delta R/R_0)/\Delta x$, where $\Delta R/R_0$ is the relative resistance change, and Δx is the beam displacement. We characterized the GC of CNT strain sensors deposited using CNT solutions of three different concentrations (0.81, 1.21, and 1.62 mg/mL). The GC at a CNT concentration of 1.62 mg/mL was 1.07 ± 0.07 mm^{-1}, which was starkly different compared to 0.19 ± 0.02 and 0.21 ± 0.02 mm^{-1} at CNT concentrations of 1.21 and 0.81 mg/mL, respectively. The distinct difference between GC values was likely attributable to different morphologies of CNT films deposited under different concentrations. As previously shown, CNT films form a two-dimensional layer when deposited at 0.81 mg/mL, while when deposited at 1.62 mg/mL, the films are thicker and resemble a three-dimensional film.[17] Two-dimensional and three-dimensional CNT films can exhibit very different electrical properties.[22]

The clot retraction force (CRF) was deduced from resistance measurements following $CRF = (\Delta R/R_0) \times (K/GC)$. The ratio of CRF to $\Delta R/R_0$, or K/GC, represents the conversion ratio from relative resistance change to CRF and thus characterizes the overall electrical measurement sensitivity. Thus, a low
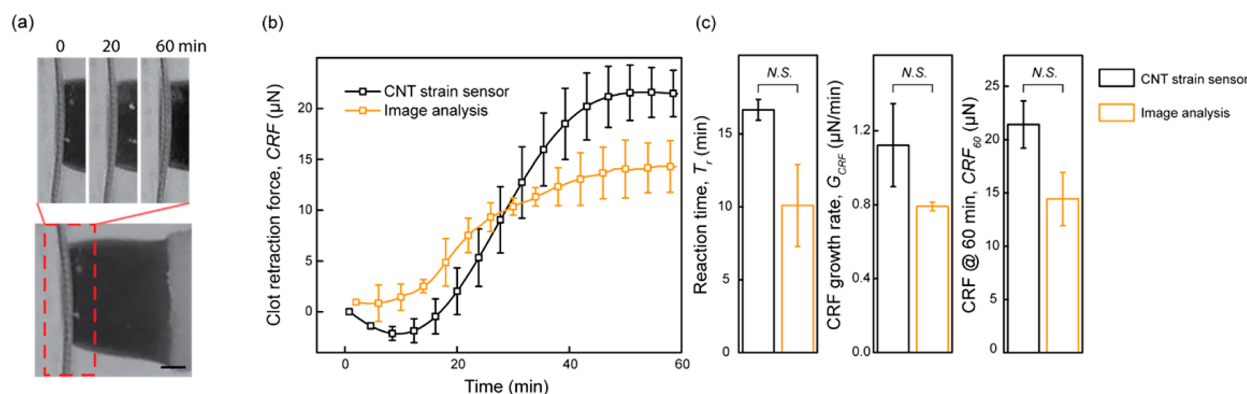
Figure 4. Comparison of CRF measurement using CNT strain sensors and image analysis. (a) Representative micrographs showing the dynamic process of blood clot formation. Scale bar, 1 mm. (b) CRF plotted as a function of time, measured from CNT strain sensor and image analysis, respectively. (c) Bar plots of reaction time T_r, growth rate G_{CRF}, and CRF_{60} of CRF dynamics measured with different methods. Data represents mean $\pm$ SEM with $n = 3$. N.S., $P > 0.05$.
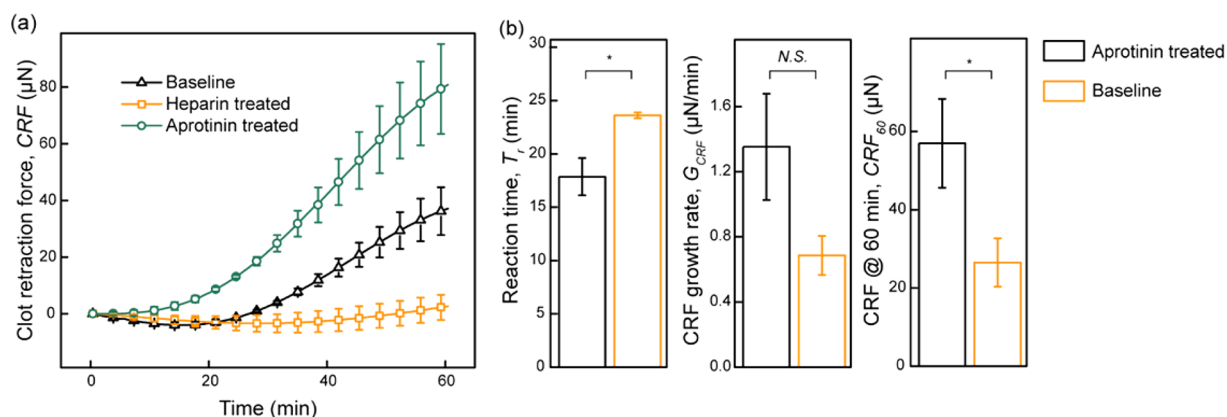

Figure 5. Effect of pro and anticoagulant on CRF measurements using CNT−mHRM devices. (a) CRF plotted as a function of time, from baseline, heparin-treated, and aprotinin-treated blood samples. (b) Bar plots of reaction time T_r, growth rate G_{CRF}, and CRF_{60} of CRF dynamics measured from aprotinin-treated and baseline blood samples. Data represents mean $\pm$ SEM with $n = 3$. *, $P < 0.05$. N.S., $P > 0.05$.

spring constant K combined with a high gauge constant GC would lead to a CNT strain sensor with heightened sensitivity. Thus, in this work, we chose to use force-sensing beam fabricated from PDMS with a Young's modulus of 0.30 MPa and a thickness of 105 μm and CNT strain sensors deposited using 1.62 mg/mL CNT solution. This combination resulted in CNT strain sensors with a sensitivity of 147.6 μN (per unit resistance change).

Comparison of CNT−mHRM with Image Analysis. We performed blood coagulation assays using CNT−mHRM devices while simultaneously optically recording displacements of the PDMS force-sensing beam, aiming to validate force measurements from the CNT strain sensor. Captured images provided a way to visually monitor blood coagulation processes as well as to calculate CRF by analyzing PDMS beam displacements from the images. As expected, CNT−mHRM devices captured dynamic clot retraction (Figure 4a) and revealed two major CRF development phases, the reaction phase and contraction development phase (Figure 4b).[3,16] From the onset of our assays ($T = 0$) to the end of reaction phase ($T = T_r$; designated as reaction time), there was an active coagulation cascade until the fibrin network was formed and activated platelets started interacting with fibrin and contracting, leading to a rapid increase of CRF in the contraction development phase. Here we defined the growth rate of CRF as

G_{CRF} and CRF at 60 min as CRF_{60}, thus $G_{CRF} = \left.\dfrac{dCRF}{dT}\right|_{T=T_r}$ and $CRF_{60} = CRF|_{T=60min}$. The reaction time T_r, CRF growth rate G_{CRF}, and CRF_{60} provide a set of parameters to assess coagulation properties of blood samples.

CNT−mHRM generated results that were comparable to those calculated from beam displacements based on image analysis. The reaction time T_r, CRF growth rate G_{CRF}, and CRF_{60} from CNT−mHRM measurements were 16.64 $\pm$ 0.71 min, 1.12 $\pm$ 0.22 μN/min, and 21.42 $\pm$ 2.22 μN, respectively, which were not significantly different compared to 10.09 $\pm$ 2.81 min, 0.79 $\pm$ 0.02 μN/min, and 14.43 $\pm$ 2.50 μN from image analysis, respectively (Figure 4). A potential factor that contributed to the discrepancy between these two methods was that in addition to blood retraction force that bent PDMS force-sensing beams, clots also applied force that was tangential to beam surfaces, which could have additional effects on electrical resistances of the CNT strain sensor.[11]

Effect of Pro and Anticoagulants on Clot Retraction Force. To demonstrate the utility of the CNT−mHRM device as a diagnostic tool for blood coagulation testing, we conducted experiments using blood samples treated with either pro or anticoagulants. Aprotinin is an inhibitor of several serine proteases such as trypsin and plasmin and thus inhibits fibrinolysis. It has been used in coronary artery bypass grafting surgery to reduce blood loss, transfusion need, and end-organ

E

damage due to hypotension.[23] Blood under the effect of aprotinin has been shown to possess elevated CRF.[24] Heparin is a glycosaminoglycan, which binds to a thrombin inhibitor, antithrombin, and increases its inhibition activity by more than 1000-fold.[25] It has been widely used as an anticoagulant (blood thinner) to treat and prevent thrombosis. Heparin can greatly inhibit blood coagulation.[26]

As shown in Figure 5, CNT−mHRM devices captured distinct CRF dynamics from untreated (baseline), aprotinin-treated, and heparin-treated blood samples. With blood samples treated with heparin, no detectable CRF was captured by the CNT−mHRM device for the entire assay duration of 60 min, which was consistent with heparin's anticoagulant function. Compared to baseline blood samples, aprotinin-treated blood samples exhibited slightly accelerated CRF development and elevated CRF at the end of the assay (CRF_{60}). The reaction time T_r from aprotinin-treated blood samples was 17.86 ± 1.75 min, which was significantly less than that of 23.61 ± 0.28 min from baseline blood samples. The CRF_{60} for aprotinin-treated blood samples was 57.00 ± 11.38 μN, which was about 2-fold of that of 26.51 ± 6.19 μN from baseline blood samples. Though the CRF growth rates between aprotinin-treated and baseline groups, which were 1.35 ± 0.33 and 0.66 ± 0.12 μN/min, respectively, were not significantly different, the three parameters combined together showed CNT−mHRM devices' capability of differentiating aprotinin-treated blood samples from baseline samples.

CONCLUSION AND DISCUSSION

In this work, we integrated CNT strain sensors into the force-sensing beam of the mHRM device and developed a new device, named CNT−mHRM, for real-time, label-free, high-throughput blood coagulation testing. This device consisted of a thin, flexible PDMS beam for force sensing and a fixed protrusion to localize blood samples. A CNT strain sensor was fabricated on top of the PDMS force-sensing beam to monitor changes of its electrical resistance and thus CRF during blood clotting. We characterized the spring constant K and GC of the force-sensing beam and performed assays on blood samples with different coagulation profiles. Results obtained from the CNT−mHRM device were consistent with those calculated from image analysis. We further demonstrated the utility of the CNT−mHRM device by performing assays on blood samples treated with drugs with known anti or procoagulation effects. The measurements were consistent with reported results, which showed the capability of the CNT−mHRM device for differentiating blood samples with different coagulation profiles. Owing to its small size, low cost, and real-time, label-free measurements, the CNT−mHRM device holds potential as a point-of-care tool for blood coagulation testing.

We should note that, however, the CNT−mHRM device tends to generate results with great interdevice variations. A few factors could have contributed to these variations. First, the fabrication process of the CNT−mHRM device involved a few manual steps, such as beam cutting and part alignment and assembly, which inevitably introduced device-to-device variations. By optimizing the device fabrication process, such as replacing manual cutting with laser cutting and adding markers to assist alignment, the variation in device fabrication could be minimized. Second, in the current form of the CNT−mHRM device, the CNT strain sensor was exposed to the environment. Disturbance from the environment, such as air flow and temperature fluctuation, could affect measurements of the CNT

strain sensor.[27] Development of a suitable packaging scheme to insulate the CNT strain sensor from the environment in the future should further improve the robustness and reliability of the CNT strain sensor and thus the CNT−mHRM device for blood coagulation testing.

ASSOCIATED CONTENT

S **Supporting Information**

The Supporting Information is available free of charge on the ACS Publications website at DOI: 10.1021/acssensors.7b00971.

> Schematic of CNT strain sensor fabrication, schematic of the experimental setup for device characterization, and spring constant plots (PDF)

AUTHOR INFORMATION

Corresponding Author

*E-mail: jpfu@umich.edu.

ORCID

Zida Li: 0000-0002-1353-9414

Jianping Fu: 0000-0001-9629-6739

Notes

The authors declare no competing financial interest.

REFERENCES

(1) Tanaka, K. A.; Key, N. S.; Levy, J. H. Blood coagulation: hemostasis and thrombin regulation. *Anesth. Analg.* **2009**, *108* (5), 1433−1446.

(2) Görlinger, K.; Dirkmann, D.; Hanke, A. A.; Kamler, M.; Kottenberg, E.; Thielmann, M.; Jakob, H.; Peters, J. First-line Therapy with Coagulation Factor Concentrates Combined with Point-of-Care Coagulation Testing Is Associated with Decreased Allogeneic Blood Transfusion in Cardiovascular SurgeryA Retrospective, Single-center Cohort Study. *Anesthesiology* **2011**, *115* (6), 1179−1191.

(3) Ganter, M. T.; Hofer, C. K. Coagulation monitoring: current techniques and clinical use of viscoelastic point-of-care coagulation devices. *Anesth. Analg.* **2008**, *106* (5), 1366−1375.

(4) Puckett, L. G.; Lewis, J. K.; Urbas, A.; Cui, X.; Gao, D.; Bachas, L. G. Magnetoelastic transducers for monitoring coagulation, clot inhibition, and fibrinolysis. *Biosens. Bioelectron.* **2005**, *20* (9), 1737−1743.

(5) Müller, L.; Sinn, S.; Drechsel, H.; Ziegler, C.; Wendel, H.-P.; Northoff, H.; Gehring, F. K. Investigation of prothrombin time in human whole-blood samples with a quartz crystal biosensor. *Anal. Chem.* **2010**, *82* (2), 658−663.

(6) Xu, W.; Appel, J.; Chae, J. Real-time monitoring of whole blood coagulation using a microfabricated contour-mode film bulk acoustic resonator. *J. Microelectromech. Syst.* **2012**, *21* (2), 302−307.

(7) Viola, F.; Mauldin, F. W.; Lin-Schmidt, X.; Haverstick, D. M.; Lawrence, M. B.; Walker, W. F. A novel ultrasound-based method to evaluate hemostatic function of whole blood. *Clin. Chim. Acta* **2010**, *411* (1), 106−113.

(8) Tripathi, M. M.; Hajjarian, Z.; Van Cott, E. M.; Nadkarni, S. K. Assessing blood coagulation status with laser speckle rheology. *Biomed. Opt. Express* **2014**, *5* (3), 817−831.

(9) Cakmak, O.; Ermek, E.; Kilinc, N.; Bulut, S.; Baris, I.; Kavakli, I.; Yaralioglu, G.; Urey, H. A cartridge based sensor array platform for multiple coagulation measurements from plasma. *Lab Chip* **2015**, *15* (1), 113−120.

(10) Maji, D.; Suster, M. A.; Kucukal, E.; Sekhon, U. D.; Gupta, A. S.; Gurkan, U. A.; Stavrou, E. X.; Mohseni, P. ClotChip: A Microfluidic Dielectric Sensor for Point-of-Care Assessment of Hemostasis. *IEEE Trans. Biomed. Circuits Syst.* **2017**, *11*, 1459.

(11) Liang, X. M.; Han, S. J.; Reems, J.-A.; Gao, D.; Sniadecki, N. J. Platelet retraction force measurements using flexible post force sensors. *Lab Chip* **2010**, *10* (8), 991−998.

(12) Lam, W. A.; Chaudhuri, O.; Crow, A.; Webster, K. D.; Li, T.-D.; Kita, A.; Huang, J.; Fletcher, D. A. Mechanics and contraction dynamics of single platelets and implications for clot stiffening. *Nat. Mater.* **2011**, *10* (1), 61−66.

(13) Myers, D. R.; Qiu, Y.; Fay, M. E.; Tennenbaum, M.; Chester, D.; Cuadrado, J.; Sakurai, Y.; Baek, J.; Tran, R.; Ciciliano, J. C.; et al. Single-platelet nanomechanics measured by high-throughput cytometry. *Nat. Mater.* **2017**, *16* (2), 230.

(14) Schwarz Henriques, S.; Sandmann, R.; Strate, A.; Köster, S. Force field evolution during human blood platelet activation. *J. Cell Sci.* **2012**, *125* (16), 3914−3920.

(15) Li, X.; Chen, W.; Li, Z.; Li, L.; Gu, H.; Fu, J. Emerging microengineered tools for functional analysis and phenotyping of blood cells. *Trends Biotechnol.* **2014**, *32* (11), 586−594.

(16) Li, Z.; Li, X.; McCracken, B.; Shao, Y.; Ward, K.; Fu, J. A miniaturized hemoretractometer for blood clot retraction testing. *Small* **2016**, *12* (29), 3926−3934.

(17) Li, Z.; Xue, X.; Lin, F.; Wang, Y.; Ward, K.; Fu, J. Capillary assisted deposition of carbon nanotube film for strain sensing. *Appl. Phys. Lett.* **2017**, *111* (17), 173105.

(18) Huang, Y. Y.; Terentjev, E. M. Dispersion of carbon nanotubes: mixing, sonication, stabilization, and composite properties. *Polymers* **2012**, *4* (1), 275−295.

(19) Sunkara, V.; Park, D.-K.; Hwang, H.; Chantiwas, R.; Soper, S. A.; Cho, Y.-K. Simple room temperature bonding of thermoplastics and poly (dimethylsiloxane). *Lab Chip* **2011**, *11* (5), 962−965.

(20) Yu, J.; Grossiord, N.; Koning, C. E.; Loos, J. Controlling the dispersion of multi-wall carbon nanotubes in aqueous surfactant solution. *Carbon* **2007**, *45* (3), 618−623.

(21) Livermore, C.; Voldman, J. Material Property Database. http://www.mit.edu/~6.777/matprops/pmma.htm (accessed December 27, 2017).

(22) Hu, L.; Hecht, D.; Grüner, G. Percolation in transparent and conducting carbon nanotube networks. *Nano Lett.* **2004**, *4* (12), 2513−2517.

(23) Mahdy, A.; Webster, N. R. Perioperative systemic haemostatic agents. *Br. J. Anaesth.* **2004**, *93* (6), 842−858.

(24) Carr, M. E.; Carr, S. L.; Roa, V.; McCardell, K. A.; Greilich, P. E. Aprotinin counteracts heparin-induced inhibition of platelet contractile force. *Thromb. Res.* **2002**, *108* (2), 161−168.

(25) Chuang, Y.-J.; Swanson, R.; Raja, S. M.; Olson, S. T. Heparin enhances the specificity of antithrombin for thrombin and factor Xa independent of the reactive center loop sequence evidence for an exosite determinant of factor Xa specificity in heparin-activated antithrombin. *J. Biol. Chem.* **2001**, *276* (18), 14961−14971.

(26) Carr, M. E., Jr; Carr, S. L.; Greilich, P. E. Heparin ablates force development during platelet mediated clot retraction. *Thrombosis and haemostasis* **1996**, *75* (4), 674−678.

(27) (a) Kim, W.; Javey, A.; Vermesh, O.; Wang, Q.; Li, Y.; Dai, H. Hysteresis caused by water molecules in carbon nanotube field-effect transistors. *Nano Lett.* **2003**, *3* (2), 193−198. (b) Yeow, J.; She, J. Carbon nanotube-enhanced capillary condensation for a capacitive humidity sensor. *Nanotechnology* **2006**, *17* (21), 5441.